This article has been accepted for publication in IEEE Transactions on Pattern Analysis and Machine Intelligence. This is the author's version which has not been fully edited and content may change prior to final publication. Citation information: DOI 10.1109/TPAMI.2023.3299526

Using Zodiacal Light For Spaceborne Calibration Of Polarimetric Imagers

Or Avitan, *Member, IEEE,* Yoav Y. Schechner, *Member, IEEE,* and Ehud Behar

Abstract—We propose that spaceborne polarimetric imagers can be calibrated, or self-calibrated using zodiacal light (ZL). ZL is created by a cloud of interplanetary dust particles. It has a significant degree of polarization in a wide field of view. From space, ZL is unaffected by terrestrial disturbances. ZL is insensitive to the camera location, so it is suited for simultaneous cross-calibration of satellite constellations. ZL changes on a scale of months, thus being a quasi-constant target in realistic calibration sessions. We derive a forward model for polarimetric image formation. Based on it, we formulate an inverse problem for polarimetric calibration and self-calibration, as well as an algorithm for the solution. The methods here are demonstrated in simulations. Towards these simulations, we render polarized images of the sky, including ZL from space, polarimetric disturbances, and imaging noise.

Index Terms—Computational photography, Polarimetric calibration, Astronomy

1 Introduction

Polarimetric cameras have various uses in computational photography [1], machine vision and scientific imaging. Examples include dynamic interferometry [2], image descattering [3], [4], [5] and lightfield imaging [6]. Polarization plays an important role in studying astronomical sources, a few outstanding examples of which are: Establishing a unified picture of obscured and unobscured sources near supermassive black holes using visible light [7], exploring the symmetry of relativistic radio jets [8], probing powerful magnetic fields in a γ-ray burst from an exploding star [9], and most recently, detecting the jet launching region from a black-hole accretion disk in X-rays [10].

As most scientific tools [11], [12], [13], [14], [15], [16], [17], [18], [19] polarimetric imagers require calibration. Polarization signals tend to be much subtler than radiance. Therefore, careful calibration is particularly needed and more challenging in polarimetry, relative to geometry and radiometry. Polarimetric calibration in a laboratory is well-established [20], [21], [22]. However, in some cases, calibration is required in the field. The reason is that outdoors, over time, instruments tend to degrade and shift away from their pre-calibrated settings. This problem is especially true for spaceborne instruments due to harsh conditions during launch and operation [23]: orbiting instruments experience extreme repetitive thermal changes in a vacuum, radiation damage, and exposure to reactive ions.

This paper focuses on polarimetric calibration and self-calibration of spaceborne imagers. Self calibration requires observing sources that have a significant degree of polarization and can cover the field of view. Polarimetric self-calibration on Earth [25], [26] focused on shiny specular objects. These are uncommon in space. Dedicated onboard calibration hardware [27], [28] requires resources that are limited or non-existent in some spacecraft. Specifically, onboard calibration requires moving parts, which may not be permitted in some satellites, due to kinetic implications and reliability risks. Some spacecraft calibrate polarimetric imagers by observing sunglint reflection on the ocean [29], [30], [31]. However, this signal is unreliable, being affected by random winds (that roughen the water) and unknown aerosol conditions. Variable aerosol conditions also affect the polarized signals reflecting from solar farms [32]. A calibrated instrument in one spacecraft can quantify a scene for *cross calibration* of another spaceborne instrument [33]. However, in optical wavelengths, currently, there are no such available systems.

Fig. 1. Zodiacal light, photographed [24] at ESO's La Silla Observatory in Chile, September 2009.

We suggest solving the problem by harnessing the polarization of a common, wide source in the solar system: the faint zodiacal light (ZL), seen in Fig. 1. ZL is created by a dust cloud measuring several astronomical units (AU), which is much larger than Earth. So, for spaceborne systems, ZL is convenient to rely on and has several advantages:

- *Or Avitan and Yoav Y. Schechner are with the Viterbi Faculty of Electrical and Computer Engineering, Technion-Israel Institute of Technology, Haifa 3200003, Israel (e-mail: avitan@campus.technion.ac.il)*
- *Ehud Behar is with the Department of Physics, Technion-Israel Institute of Technology, Haifa 3200003, Israel*

This work is licensed under a Creative Commons Attribution 4.0 License. For more information, see https://creativecommons.org/licenses/by/4.0/

This article has been accepted for publication in IEEE Transactions on Pattern Analysis and Machine Intelligence. This is the author's version which has not been fully edited and content may change prior to final publication. Citation information: DOI 10.1109/TPAMI.2023.3299526

ZL is insensitive to the camera location, say, of a satellite in low Earth orbit (LEO) [34]. Hence, ZL can be used to simultaneously calibrate a constellation of orbiting satellites. From space, ZL is unaffected by atmospheric scattering or other terrestrial disturbances. ZL has a significant degree of linear polarization (DoLP) in a wide field of view. Its signal changes very slowly in time, on the scale of months, as the dust cloud orbits the sun. It is thus a quasi-constant target in realistic calibration sessions. Using ZL, allows for calibration far from Earth, in deep space missions to other planets or asteroids. We do not, however, recommend ZL as a calibration source on Earth, due to atmospheric interference.

This paper is the first to propose ZL as a source for polarimetric calibration. We derive a forward model for image formation. Based on the model, we formulate an inverse problem for polarimetric calibration and self-calibration in space. The paper then presents an algorithm for a solution.[1] The present work is timely, as in the coming years, several polarimetric imagers are expected to be launched to LEO [34], [35], [36]: Using these planned imagers, these methods can be demonstrated empirically. Meanwhile, the methods here are demonstrated in simulations. Toward these simulations, we create a simulator to render ad-hoc polarized images of the sky (including ZL) from space, accounting for noise and polarimetric disturbances.

2 Theoretical Background

2.1 Interplanetary Dust

Zodiacal light (ZL) is seen Fig. 1. It is created by the scattering of sunlight and by thermal self-emission from interplanetary dust particles (IDPs). Sources of IDPs include comet dust, asteroidal dust, Kuiper belt dust, and interstellar dust. Interplanetary dust is significant for understanding the formation and evolution of our solar system and others [37].

IDPs have been studied by several space missions, including the Infrared Astronomical Satellite (IRAS) [38], the Cosmic Background Explorer (COBE) [39], and the Infrared Space Observatory (ISO) [40]. These and additional studies [41], [42], [43] advanced knowledge of the dust's spatial distribution of density, temperature and microphysics (albedo, shape, size distribution, refractive index, chemical content). IDPs are often made of silicate or carbonaceous materials such as graphite. Typical IDP sizes range from fractions of μm up to tens of μm.

IDPs mainly reside in a non-uniform cloud [44], concentrated in and near the ecliptic plane (which includes Earth's orbit). The Kelsall model [45] describes the IDP cloud, based on components having various spatial and dynamical properties. Based on this model, the dust density is illustrated in Fig. 2. The cloud is dynamic, as each IDP is subject to gravitational forces, radiation pressure, and Poynting–Robertson drag (a radiative process that causes an IDP to lose angular momentum [46]). From Earth, in the short-wave infrared range [46], the optical depth of the IDP cloud is $\sim 5 \cdot 10^{-8}$, for absorption and scattering.

1. Our code is available at https://github.com/oravitan/zodiacal-polarized

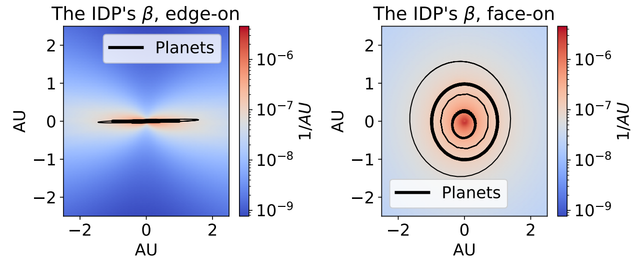

Fig. 2. Edge-on (left) and face-on (right) cross-sections of the extinction coefficient β of the IDPs, based on the Kelsall model.

2.2 Zodiacal Light

The IDP cloud is mainly concentrated between the sun and the asteroid belt. IDP density, irradiance, and temperature decrease with distance from the sun (the temperature is $\sim 250°\mathrm{K}$ near Earth [46]). Hence, ZL is brighter near the sun. As a result, from Earth, ZL can be seen by the naked eye near the horizon, around the ecliptic, for a short time after sunset and before dawn (See Fig. 1). It is very faint, thus observations require being away from stray light and atmospheric pollution sources, especially towards the horizon. Using long exposures, ZL is measured at night from ground stations [47]. The best way to observe it, of course, is to be in space, away from of any light pollution created by atmospheric scattering and devoid of atmospheric attenuation. This paper uses spaceborne imaging of ZL, thus the optical models we use have no atmospheric contribution.

Thermal self-emission is unpolarized and it is dominant only in long-wave infrared. The visible and near-infrared spectrum of ZL is similar to that of sunlight, which IDPs scatter. This scattering is partially polarized (ZL DoLP is as high as 20%), which benefits our calibration goal. The DoLP is typically higher in viewing directions where the ZL is fainter [37].

2.3 Zodiacal Light Model

Due to the low optical depth of the IDP cloud, the model of ZL radiance resembles a haze model as in [48], [49], having single scattering of sunlight and background of planets and stars, in addition to thermal self-emission.

Let $\mathbf{X}$ denote location in 3D space. Let λ denote wavelength. The spectral radiance from a region around $\mathbf{X}$ is $L_{\text{scene}}(\mathbf{X}, \lambda)$. The IDP cloud is comprised of various components, created by various sources (comets, asteroids, etc.). Index a component by $\kappa = 1 \ldots N_{\text{comp}}$. The cloud is optically very thin, hence components practically do not attenuate or scatter each other. Hence their contribution to the spectral radiance of the scene is additive:

$$L_{\text{scene}}(\mathbf{X}, \lambda) = \sum_{\kappa=1}^{N_{\text{comp}}} L_{\kappa}(\mathbf{X}, \lambda) \quad \left[\frac{W}{m^2 \cdot sr \cdot \mu m \cdot \mathrm{AU}}\right] . \quad (1)$$

We now describe how each component is expressed. Each component has spatially varying, wavelength-dependent particle albedo $A_{\kappa,\mathbf{X},\lambda}$, phase function $\Phi_{\kappa,\mathbf{X},\lambda}$ $\left[sr^{-1}\right]$ and temperature $T_{\kappa,\mathbf{X},\lambda}$. The extinction coefficient (including both scattering and absorption) $\beta_{\kappa,\mathbf{X},\lambda}$ has units of AU^{-1}. IDPs are illuminated by solar flux density $F_{\mathbf{X},\lambda}$ in units

This work is licensed under a Creative Commons Attribution 4.0 License. For more information, see https://creativecommons.org/licenses/by/4.0/

This article has been accepted for publication in IEEE Transactions on Pattern Analysis and Machine Intelligence. This is the author's version which has not been fully edited and content may change prior to final publication. Citation information: DOI 10.1109/TPAMI.2023.3299526

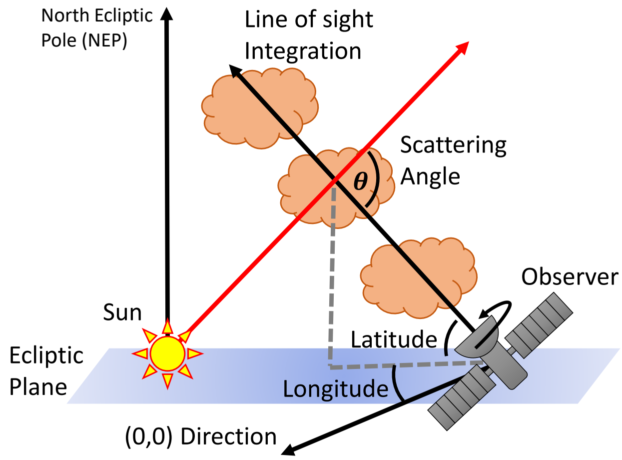

Fig. 3. Line of sight scattering integration.

of $\frac{W}{m^2 \cdot \mu m}$. Let $h, c, \mathrm{k^B}$ denote Planck's constant, the speed of light in vacuum, and Boltzmann's constant, respectively. Thermally emitted radiance by IDPs is approximately described by black body radiation, proportional to

$$B_{\kappa,\mathbf{X},\lambda} = \frac{2hc^2}{\lambda^5 \left[\exp(hc/\mathrm{k^B}\lambda T_{\kappa,\mathbf{X},\lambda}) - 1\right]} \quad \left[\frac{W}{m^2 \cdot sr \cdot \mu m}\right]. \tag{2}$$

Deviations from the black body model are expressed [45] by a unitless emissivity $E_{\kappa,\lambda}$.

Accounting both for scattering and self-emission [45], the volumetric spectral radiance of component κ from a region around $\mathbf{X}$ and wavelength λ is

$$L_\kappa(\mathbf{X}, \lambda) = \beta_\kappa[A_\kappa F \Phi_\kappa + (1 - A_\kappa) E_\kappa B_\kappa], \tag{3}$$

where we omitted the $\mathbf{X}, \lambda$ subscripts on the right-hand side, for brevity. Due to the very low optical depth of the IDP cloud, neglecting the attenuation is valid along any line of sight (LOS) $\mathcal{L}$, and between $\mathbf{X}$ and the sun. The ZL is obtained by LOS integration of $L_{\text{scene}}(\mathbf{X}, \lambda)$ along $\mathcal{L}$:

$$I_{\text{ZL}}(\mathcal{L}, \lambda) = \int_{\mathbf{X} \in \mathcal{L}} L_{\text{scene}}(\mathbf{X}, \lambda) d\mathbf{X} \quad \left[\frac{W}{m^2 \cdot sr \cdot \mu m}\right]. \tag{4}$$

This is illustrated in Fig. 3.

Kelsall's Model

The Kelsall model [45] sets the parameters above, for short-wave infra-red bands. The model is based on IRAS, COBE, and ISO data, and is designed to yield unpolarized ZL radiance expressed in Eq. (4). The IDP density stemming from this model is illustrated in Fig. 2. Let $\mathbf{X}_\odot$ be the location of the Sun and $\mathbf{X}_\mathrm{C}$ be the location of the camera. The direction along $\mathcal{L}$ is $\hat{\mathcal{L}} = [\mathbf{X} - \mathbf{X}_\mathrm{C}]/\|\mathbf{X} - \mathbf{X}_\mathrm{C}\|$. Solar illumination at a voxel is $\hat{\mathbf{d}}_\odot = [\mathbf{X} - \mathbf{X}_\odot]/\|\mathbf{X} - \mathbf{X}_\odot\|$. Then, the scattering angle is

$$\theta(\mathbf{X}) = \arccos(-\hat{\mathcal{L}} \cdot \hat{\mathbf{d}}_\odot) \, . \tag{5}$$

In the Kelsall model, the unpolarized phase function for scattering at angle θ is parameterized by

$$\Phi^{\text{kelsall}}_{\kappa,\lambda}(\theta) = C^{(0)}_{\kappa,\lambda} + C^{(1)}_{\kappa,\lambda}\theta + \exp(C^{(2)}_{\kappa,\lambda}\theta). \tag{6}$$

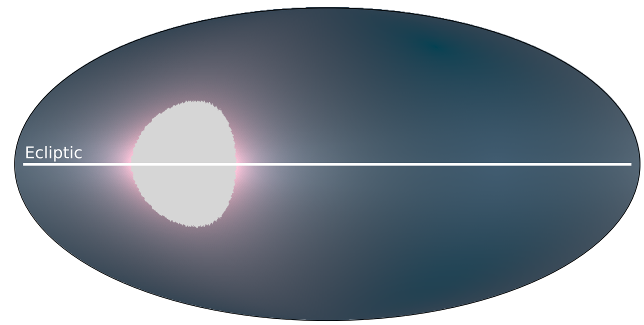

Fig. 4. Zodiacal light full-sky image as seen from earth, based on the Kelsall model, false-colored: $\lambda = 1.25\mu m, 2.2\mu m, 3.5\mu m$ are represented by RGB (channels stretched each to [0,1], then gamma-corrected with $\gamma = 0.25$), simulated for June 14th, 2022, in Mollweide projection. The area around the sun is excluded (gray).

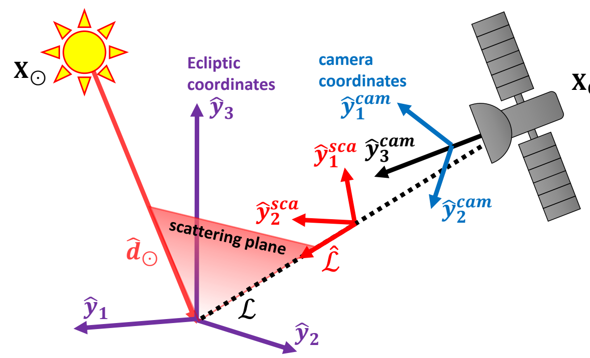

Fig. 5. The three dimensional coordinate systems.

The parameters $C^{(0)}_{\kappa,\lambda}, C^{(1)}_{\kappa,\lambda}, C^{(2)}_{\kappa,\lambda}$ are fitted to data that had been sensed at $\lambda = 1.25\mu m, 2.2\mu m, 3.5\mu m$, while the phase function is normalized. This modeled phase function is consistent with measurements of the ZL [37].

To demonstrate this, we ran the model of Eqs. (1,2,3,4,6). Full-sky image results are shown in Fig. 4. The visualization here is in the Mollweide projection, where the central point is at $(\text{lon}, \text{lat}) = (0, 0)$ in ecliptic coordinates, directed towards the vernal equinox.

3 Forward Model

3.1 Three-dimensional (3D) Coordinate systems

We use several 3D right-handed coordinate systems [50] (See Fig. 5).

- The *ecliptic* system has axes $\hat{\mathbf{y}}_1 \perp \hat{\mathbf{y}}_2 \perp \hat{\mathbf{y}}_3$. Axis $\hat{\mathbf{y}}_1$ is in the ecliptic plane, pointing to the vernal equinox. Axis $\hat{\mathbf{y}}_3$ is perpendicular to the ecliptic plane, pointing to the north ecliptic pole.
- In the *camera* system, axis $\hat{\mathbf{y}}_3^{\text{cam}}$ aligns with the optical axis of the camera. Axes $\hat{\mathbf{y}}_1^{\text{cam}}, \hat{\mathbf{y}}_2^{\text{cam}}$ are orthogonal to $\hat{\mathbf{y}}_3^{\text{cam}}$ and align with the sensor rows and columns, respectively.
- The *scattering* system is set by the *scattering plane* which contains the sun's projection $[\mathbf{X}_\mathrm{C} - \mathbf{X}_\odot]/\|\mathbf{X}_\mathrm{C} - \mathbf{X}_\odot\|$ and $\mathcal{L}$. The system axes are $\hat{\mathcal{L}}$ and

$$\hat{\mathbf{y}}_1^{\text{sca}} = \hat{\mathcal{L}} \times \frac{\mathbf{X}_\mathrm{C} - \mathbf{X}_\odot}{\|\mathbf{X}_\mathrm{C} - \mathbf{X}_\odot\|}, \quad \hat{\mathbf{y}}_2^{\text{sca}} = \hat{\mathcal{L}} \times \hat{\mathbf{y}}_1^{\text{sca}} \, . \tag{7}$$

This work is licensed under a Creative Commons Attribution 4.0 License. For more information, see https://creativecommons.org/licenses/by/4.0/

This article has been accepted for publication in IEEE Transactions on Pattern Analysis and Machine Intelligence. This is the author's version which has not been fully edited and content may change prior to final publication. Citation information: DOI 10.1109/TPAMI.2023.3299526

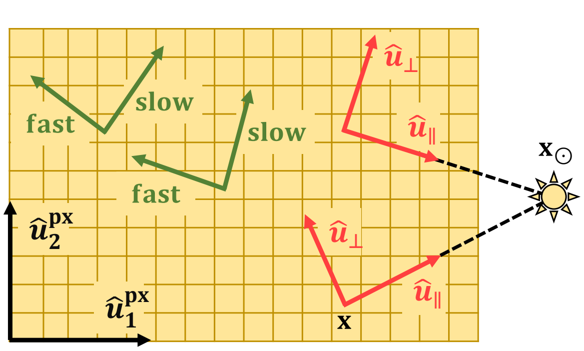

Fig. 6. The two dimensional coordinate systems.

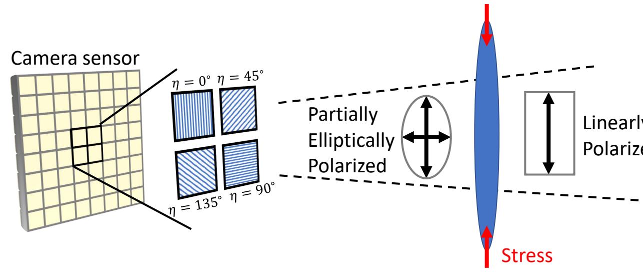

Fig. 7. Imaging optics may induce depolarization, particularly due to birefringence created by stress, that is exacerbated by thermal changes. This leads to partial mixing of polarization components. Due to the system's point spread function, light along LOS $\mathcal{L}$ is spread over a set of sensor pixels. Each sensor pixel is covered by a small polarizing filter. The filter angle η depends (and is known) on the sensor pixel location.

Rotation between 3D coordinate systems is described by a 3×3 rotation matrix $\mathbf{G}$. The matrix $\mathbf{G}_{\text{cam}}$ transforms directions in the ecliptic system, where astronomical data are defined, to the camera system, where images are projected. For more details on 3D coordinate systems in conjunction to polarimetric sensor arrays, see [50].

3.2 Two-dimentional (2D) Coordinate systems

We use 2D coordinate systems (see Fig. 6):

- The *pixel* system, defined by $\hat{\mathbf{u}}_1^{\text{px}} \perp \hat{\mathbf{u}}_2^{\text{px}}$, which aligns with the rows and columns of the pixel array.
- The *projected scattering* system, defined by $\hat{\mathbf{u}}_{\parallel} \perp \hat{\mathbf{u}}_{\perp}$. The vector $\hat{\mathbf{u}}_{\parallel}$ aligns with the projection of the *scattering plane* to the image plane. The scattering plane includes the sun, which projects to 2D location $\mathbf{x}_{\odot}$ on the image plane. LOS $\mathcal{L}$ projects to a pixel at $\mathbf{x}$. Hence, $\hat{\mathbf{u}}_{\parallel} = [\mathbf{x}_{\odot} - \mathbf{x}] \,/\, \|\mathbf{x}_{\odot} - \mathbf{x}\|$. The angle between the *projected scattering* and *pixel* coordinate systems is α^{cam}. As seen in Fig. 6, α^{cam} is a function of the pixel location $\mathbf{x}$.
- A *retarder* coordinate system, which is useful for describing birefringence. The system is defined by two orthogonal axes: light polarized in one axis experiences a higher refractive index (slow) than light polarized in the other (fast) [51] axis. The fast component has angle α_{br} relative to the *pixel* coordinate system. As seen in Fig. 6, α_{br} is generally a smooth function of the pixel location $\mathbf{x}$.

Light that is partially linearly polarized is expressed by a three-element Stokes vector. Let $\top$ denote transposition. The scene Stokes vector projected by LOS $\mathcal{L}$ is

$$\boldsymbol{s}_{\mathcal{L}}(\lambda) = [I_{\mathcal{L}}(\lambda)\; Q_{\mathcal{L}}(\lambda)\; U_{\mathcal{L}}(\lambda)]^{\top} \,. \tag{8}$$

Here the scene's radiance is $I_{\mathcal{L}}(\lambda)$, while its angle of polarization is associated with the ratio of $Q_{\mathcal{L}}$ and $U_{\mathcal{L}}$. In ZL, the angle of polarization is set by the scattering plane. We then represent this angle (thus the ratio of $Q_{\mathcal{L}}$ and $U_{\mathcal{L}}$) in the *projected scattering* coordinate system.

Transforming a Stokes vector from any 2D coordinate system to another is a rotation by angle α, expressed by a Mueller rotation matrix

$$\mathbf{R}(\alpha) = \begin{bmatrix} 1 & 0 & 0 \\ 0 & \cos(2\alpha) & \sin(2\alpha) \\ 0 & -\sin(2\alpha) & \cos(2\alpha) \end{bmatrix} . \tag{9}$$

3.3 Polarimetric Imaging

Propagating through the camera's optical elements, as shown in Fig. 7, light polarization may be affected by birefringence [20]. This is a particular concern in LEO, as mentioned in Sec. 1. Generally, a LEO satellite is periodically either heated strongly by direct solar illumination or exposed to extremely low temperatures of space, in Earth's shadow. Thermal variations lead to temporal changes of stress on the optical system [52]. These, in turn, may cause birefringence that varies gradually in orbit. Birefringence mixes polarization components and is typically modeled as a linear retarder. A retarder has phase retardance δ between the fast and slow components (Sec. 3.2). In the *retarder coordinate system* the birefringence Mueller matrix is

$$\mathbf{M}_{\text{br}}(\delta) = \begin{bmatrix} 1 & 0 & 0 \\ 0 & 1 & 0 \\ 0 & 0 & \cos\delta \end{bmatrix} . \tag{10}$$

In the *pixel coordinate system*, a birefringence Muller matrix is

$$\mathbf{B}(\delta, \alpha_{\text{br}}) = \mathbf{R}^{-1}(\alpha_{\text{br}})\mathbf{M}_{\text{br}}(\delta)\mathbf{R}(\alpha_{\text{br}}) \,. \tag{11}$$

Let

$$\mathtt{a} = \cos^2(2\alpha_{\text{br}}) + \cos\delta \sin^2(2\alpha_{\text{br}}) \,, \tag{12}$$

$$\mathtt{b} = \cos(2\alpha_{\text{br}})\sin(2\alpha_{\text{br}})(1 - \cos\delta) \,, \tag{13}$$

$$\mathtt{c} = \sin^2(2\alpha_{\text{br}}) + \cos\delta \cos^2(2\alpha_{\text{br}}) \,. \tag{14}$$

From Eqs. (9,10,12,13,14),

$$\mathbf{B}(\delta, \alpha_{\text{br}}) = \begin{bmatrix} 1 & 0 & 0 \\ 0 & \mathtt{a} & \mathtt{b} \\ 0 & \mathtt{b} & \mathtt{c} \end{bmatrix}_{3\times 3} . \tag{15}$$

Recall that $\boldsymbol{s}_{\mathcal{L}}(\lambda)$ in Eq. (8) is expressed in the *projected scattering* coordinate system. Transferring $\boldsymbol{s}_{\mathcal{L}}(\lambda)$ to the pixel coordinate system and then passing through optical imaging (lens) elements yields

$$\boldsymbol{s}_{\text{pre}}(\mathcal{L}, \lambda) = \mathbf{B}(\delta, \alpha_{\text{br}})\mathbf{R}(\alpha^{\text{cam}})\boldsymbol{s}_{\mathcal{L}}(\lambda) \,, \tag{16}$$

based on Eqs. (8,9,10,11). This is the Stokes vector of light heading towards the detector (sensor) array. Consider cameras where each sensor pixel has an attached linear polarizer [2], [50]. Let $\mathbf{x}(\mathcal{L})$ be a pixel on the sensor array, to which

This work is licensed under a Creative Commons Attribution 4.0 License. For more information, see https://creativecommons.org/licenses/by/4.0/

This article has been accepted for publication in IEEE Transactions on Pattern Analysis and Machine Intelligence. This is the author's version which has not been fully edited and content may change prior to final publication. Citation information: DOI 10.1109/TPAMI.2023.3299526

LOS $\mathcal{L}$ projects. A pixel is covered by a tiny polarizing filter at angle η relative to the rows of the pixel array. The filter has polarizance $P \leq 1$. After light passes the filter, it yields a signal equivalent to radiance

$$I_{\text{cam}}[\mathbf{x}(\mathcal{L}), \lambda, \eta] = \begin{bmatrix} \frac{1}{2} & \frac{P\cos(2\eta)}{2} & \frac{P\sin(2\eta)}{2} \end{bmatrix} \boldsymbol{s}_{\text{pre}}(\mathcal{L}, \lambda), \tag{17}$$

in units of $\frac{W}{m^2 \cdot sr \cdot \mu m}$. The optical system's point spread function spans several sensor pixels, thus the signal of $\mathcal{L}$ spreads (not spatially resolved) over several nearby pixels. Term *super-pixel* a 2×2 set of adjacent sensor pixels. The polarizer angles in this set are $\eta = 0°, 45°, 90°, 135°$. Their polarizance is P. Because the signal irradiating the sensor pixels is the same within the super-pixel, we assign the whole super-pixel the location $\mathbf{x}$. Then, from Eq. (17).

$$\begin{bmatrix} I_{\text{cam}}[\mathbf{x}(\mathcal{L}), \lambda, 0°] \\ I_{\text{cam}}[\mathbf{x}(\mathcal{L}), \lambda, 45°] \\ I_{\text{cam}}[\mathbf{x}(\mathcal{L}), \lambda, 90°] \\ I_{\text{cam}}[\mathbf{x}(\mathcal{L}), \lambda, 135°] \end{bmatrix} = \mathbf{V}\boldsymbol{s}_{\text{pre}}(\mathcal{L}, \lambda) , \tag{18}$$

where

$$\mathbf{V} = \frac{1}{2} \begin{bmatrix} 1 & P & 0 \\ 1 & 0 & P \\ 1 & -P & 0 \\ 1 & 0 & -P \end{bmatrix}_{4 \times 3} . \tag{19}$$

3.4 Light to Electrons

The radiance obtained by Eq. (17) is converted to model an expected signal $\bar{N}[\mathbf{x}(\mathcal{L})]$ and noise in photoelectrons, as in [50]. A light detector is sensitive to a narrow spectral band Λ. Let $p, \Delta t, D, f$ be the camera's pixel length, exposure time, lens diameter, and focal length. The optical train has transmittance τ_λ. This accounts also for imperfect transmissivity by a polarizer aligned with the polarization of an incoming field. A pixel has quantum efficiency QE_λ. Radiance $I_{\text{cam}}(\mathbf{x}, \lambda, \eta)$ corresponding to $\mathbf{x}$ yields an expected number of photo-electrons

$$\bar{N}(\mathbf{x}, \eta) = \int_\Lambda \Gamma_\lambda I_{\text{cam}}(\mathbf{x}, \lambda, \eta) d\lambda , \tag{20}$$

where

$$\Gamma_\lambda = \pi \Delta t \tau_\lambda \left(\frac{D}{2f}\right)^2 \text{QE}_\lambda \frac{\lambda}{hc} p^2 \quad \left[\frac{m^2 sr}{J}\right]. \tag{21}$$

In a practical camera, Γ_λ expresses specifications that are known following *unpolarized* calibration of radiometry [53], [54] and geometry [55], [56]. These methods are well established, specifically from LEO. The polarized parameters constitute a set $\Psi_{\mathbf{x}} \equiv \{\mathtt{a}, \mathtt{b}, \mathtt{c}, P\}$. A vector of the expected number of photo-electrons from the four-pixel elements in a super-pixel is

$$\bar{\boldsymbol{n}}(\mathbf{x}) = \left[\bar{N}(\mathbf{x}, 0°),\ \bar{N}(\mathbf{x}, 45°),\ \bar{N}(\mathbf{x}, 90°),\ \bar{N}(\mathbf{x}, 135°)\right]^\top . \tag{22}$$

A scene is a *map* $\mathcal{S} \equiv \{\boldsymbol{s}_\mathcal{L}(\lambda)\}_{\forall \mathcal{L}, \lambda}$ of all Stokes vectors of the scene, in all potential viewing directions and relevant wavelengths. A measurement at a state of the spacecraft is indexed by k. There are K measurements, each yielding a 4-element vector $\bar{\boldsymbol{n}}(\mathbf{x})$ per $\mathbf{x}$, as in Eq. (22). Per k, the camera is oriented differently, thus a different LOS $\mathcal{L}(k)$ projects to super-pixel $\mathbf{x}$. Denote this projection by $\mathcal{L}(k) \to \mathbf{x}$. Then, super-pixel $\mathbf{x}$ measures per k a Stokes vector

$$\boldsymbol{s}_k(\mathbf{x}) = \boldsymbol{s}\{\mathcal{L}(k) \to \mathbf{x}\} . \tag{23}$$

Using Eqs. (16,17,18,19,20,22,23), the forward model is

$$\bar{\boldsymbol{n}}_k = \int_\Lambda \Gamma_\lambda \mathbf{V}\mathbf{B}\mathbf{R}_k \boldsymbol{s}_k(\lambda) d\lambda \ \ [\text{electrons}] , \tag{24}$$

where $\mathbf{R}_k = \mathbf{R}(\alpha_k^{\text{cam}})$, and $\bar{\boldsymbol{n}}_k$ is a 4-element column vector. Define a Stokes vector aggregated over the spectral band as

$$\tilde{\boldsymbol{s}}_k = \begin{bmatrix} \tilde{I}_k \\ \tilde{Q}_k \\ \tilde{U}_k \end{bmatrix} \equiv \int_\Lambda \Gamma_\lambda \boldsymbol{s}_k(\lambda) d\lambda \quad [\text{electrons}] . \tag{25}$$

We assume $\Psi_{\mathbf{x}}$ is insensitive to λ within Λ. From Eq. (24,25),

$$\bar{\boldsymbol{n}}_k = \mathbf{V}\mathbf{B}\mathbf{R}_k \tilde{\boldsymbol{s}}_k \ \ [\text{electrons}] . \tag{26}$$

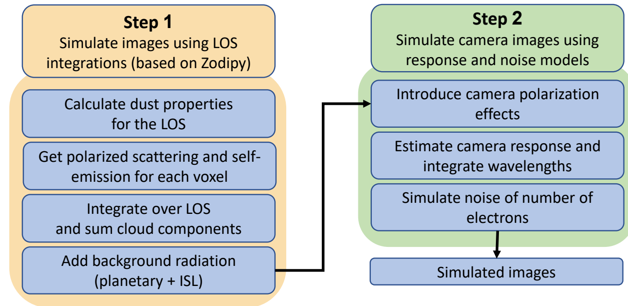

Fig. 8. Rendering partially polarized sky images, including ZL.

4 Rendering The LEO Polarized Sky

The main goal of this paper is to solve an inverse problem based on data acquired in space, rather than rendering. However, to test some of our hypotheses using simulations, we prefer to have a rendering model. This can serve us in simulating celestial polarization images as if taken by a spaceborne camera pointing away from Earth. We stress that this section is not a part of our principle and calibration methods. A reader uninterested in rendering, but seeks solely calibration, can skip directly to Sec. 5.

Some rendering models [57] use average ZL maps from 1968, oblivious to spatiotemporal ZL variability. Our rendering flow is summarized in Fig. 8. Secs. 3.3 and 3.4 convert a spectral Stokes vector along a scene LOS $\boldsymbol{s}_\mathcal{L}(\lambda)$, to a camera signal. This section models $\boldsymbol{s}_\mathcal{L}(\lambda)$ in an ad-hoc manner.

From Eq. (8), the first component in $\boldsymbol{s}_\mathcal{L}(\lambda)$ is the scene intensity $I_\mathcal{L}(\lambda)$. Eq. (4) expresses the ZL intensity along $\mathcal{L}$. However, a LOS $\mathcal{L}$ also observes background planets, stars, and other objects, e.g., galaxies. Extra-solar objects are accounted for by integrated starlight (ISL), $I_{\text{ISL}}(\mathcal{L})$. In our solar system, each planet p has radiance $I_{\text{p}}^{\text{planet}}(\lambda)$. Overall,[2] the radiance reaching the camera in units of $\frac{W}{m^2 \cdot sr \cdot \mu m}$ is

$$I_\mathcal{L}(\lambda) = I_{\text{ZL}}(\mathcal{L}, \lambda) + I_{\text{ISL}}(\mathcal{L}, \lambda) + \sum_{\text{p} \in \mathcal{L}} I_{\text{p}}^{\text{planet}}(\lambda) . \tag{27}$$

2. Additional background radiation sources exist, but they can be neglected in our context.

This work is licensed under a Creative Commons Attribution 4.0 License. For more information, see https://creativecommons.org/licenses/by/4.0/

This article has been accepted for publication in IEEE Transactions on Pattern Analysis and Machine Intelligence. This is the author's version which has not been fully edited and content may change prior to final publication. Citation information: DOI 10.1109/TPAMI.2023.3299526

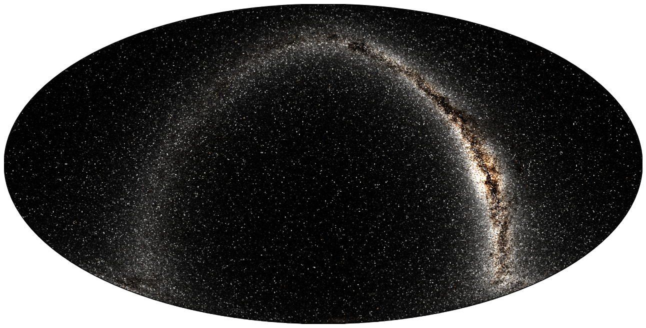

Fig. 9. The integrated starlight model in full-sky view (real-color in logarithmic scale), simulated for June 14th, 2022, in Mollweide projection.

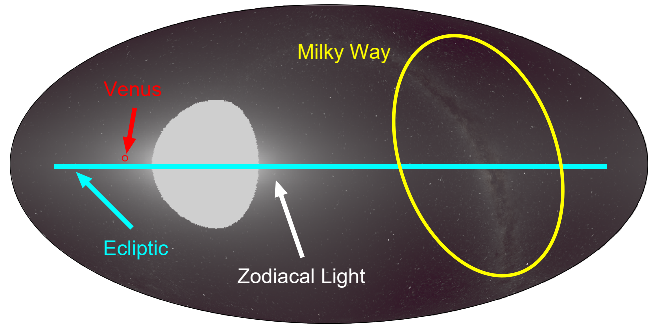

Fig. 10. Full Sky simulated color image (gamma corrected with $\gamma = 0.4$), simulated for June 1st, 2023, in Mollweide projection.

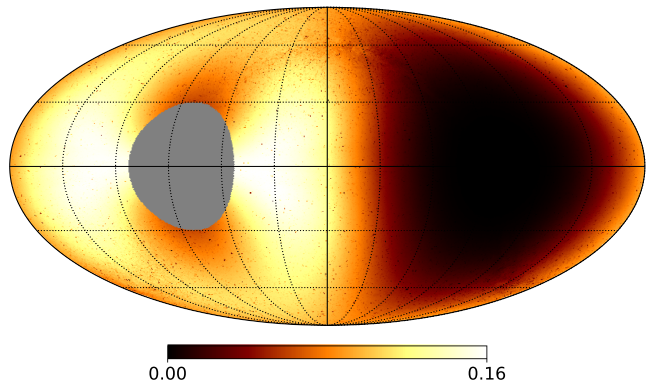

Fig. 11. Full sky DoLP image (red channel), simulated for June 14th, 2022, in Mollweide projection.

Eq. (4) requires $L_{\text{scene}}(\mathbf{X}, \lambda)$. However, the Kelsall model is only given in short-wave infrared, not visible light. Our literature search did not find a satisfactory model for visible light. We found several ad-hoc approximations, which we use. First, in Kelsall's model, the extinction coefficient is insensitive to the wavelength, and indeed, many long exposure images of ZL show it rather colorless. Hence, we use $\beta_{\kappa,\mathbf{X}}$ as in the Kelsall model. Second, the unpolarized phase function is extrapolated in the wavelength domain. LOS integration over dust properties is performed by the Zodipy library [58].

We model the non-ZL components similarly to [42]. For the ISL, object locations and multi-spectral magnitudes are found by the Two Micron All Sky Survey (2MASS) [59] catalog using AstroQuery [60]. The multi-spectral magnitudes are fit to Eq. (2), yielding star temperatures and emissions of visible light. Afterward, we sample these bodies in every direction by Monte-Carlo simulation and integration. This yields $I_{\text{ISL}}(\mathcal{L}, \lambda)$, as shown in Fig. 9.

Per date, the location $\mathbf{X}_{\text{p}}$ of planet p is obtained using Ephemeris from Astropy [61]. A planet has radius R_{p}. The Bond albedo $\mathtt{K}_{\text{p}}$ is the fraction of incident power that is scattered back to space. The solar spectral flux density at planet p is $F_{\text{p},\lambda}$, as in Eq. (3). The scattering angle between the vector of solar irradiance and the direction from the planet to the camera is θ_{p}. Then [62],

$$I_{\text{p}}^{\text{planet}}(\lambda) = \frac{2\mathtt{K}_{\text{p}}}{3} \frac{R_{\text{p}}^2}{\|\mathbf{X}_{\text{p}} - \mathbf{X}_{\mathtt{C}}\|_2^2} F_{\text{p},\lambda} \left[\sin\theta_{\text{p}} - \theta_{\text{p}}\cos\theta_{\text{p}}\right] . \quad (28)$$

An example for the overall $I_{\mathcal{L}}$ (Eq. 27) is shown in Fig. 10.

Next, we assign the polarized components $Q_{\mathcal{L}}(\lambda), U_{\mathcal{L}}(\lambda)$ of Eq. (8). ISL is assumed to have negligible[3] polarization [42]. Planetary light can be polarized, but we use the planets only for geometric calibration, hence we do not model planetary polarization. Thus, $Q_{\mathcal{L}}(\lambda), U_{\mathcal{L}}(\lambda)$ depend only on the ZL. For ZL, the angle of polarization $\text{AoP}_{\mathcal{L}}$ is known: it is perpendicular to the scattering plane, per $\mathcal{L}$. Hence, in the *projected scattering* coordinate system

$$\boldsymbol{s}_{\mathcal{L}} = \left[I_{\mathcal{L}}(\lambda)\ Q_{\mathcal{L}}(\lambda)\ 0\right]^{\top} . \quad (29)$$

3. Resolvable stars are essentially point sources that cover a tiny fraction of the field of view. Stars are intrinsically unpolarized. Some star observations sense DoLP $\sim [1-2\%]$, due to iron grains in interstellar dust that align with interstellar magnetic fields [63], [64], [65]. This small effect is seen mainly in the galactic plane, that is, in the bright band of the Milky Way. If we wish to avoid (rather than use) this effect, we may direct our imager away from this bright band.

The component $Q_{\mathcal{L}}(\lambda)$ is associated with the corresponding ZL component, which is modeled analogously to Eqs. (1,4):

$$Q_{\mathcal{L}}(\lambda) \sim Q_{\text{ZL}}(\mathcal{L}, \lambda) = \int_{\mathbf{X}\in\mathcal{L}} \sum_{\kappa=1}^{N_{\text{comp}}} L_{\kappa}^{\text{Q}}(\mathbf{X}, \lambda) d\mathbf{X} . \quad (30)$$

Here $L_{\kappa}^{\text{Q}}(\mathbf{X}, \lambda)$ is the polarized component of scattered light at $\mathbf{X}$. It is derived in analogy[4] to Eq. (3)

$$L_{\kappa}^{\text{Q}}(\mathbf{X}, \lambda) = \beta_{\kappa,\mathbf{X},\lambda} A_{\kappa,\mathbf{X},\lambda} F_{\mathbf{X},\lambda} \Phi_{\kappa,\lambda} \text{DoLP}_{\text{IDP}}[\theta(\mathbf{X})] , \quad (31)$$

where $\text{DoLP}_{\text{IDP}}[\theta(\mathbf{X})]$ is the degree of linear polarization of light scattered at $\mathbf{X}$, and $\theta(\mathbf{X})$ is defined in Eq. (5). Note that $\text{DoLP}_{\text{IDP}}[\theta(\mathbf{X})]$ depends on the IDPs in voxel $\mathbf{X}$. An approximation that fits empirical visible-range data [66] is

$$\text{DoLP}_{\text{IDP}}[\theta] = 0.33 \sin^5\theta . \quad (32)$$

A camera senses an integral over a LOS (Eq. 30). The DoLP of light reaching the camera is $Q_{\mathcal{L}}(\lambda)/I_{\mathcal{L}}(\lambda)$. Eqs. (30,31,32) yield the polarized component of the Stokes vector.

5 Polarimetric Calibration by ZL

Equation (26) provides a forward model for imaging. This paper seeks an estimation of the camera's polarization set of parameters $\Psi_{\mathbf{x}}$, $\forall\mathbf{x}$. The main question is whether $\mathcal{S}$ is known, or at least modeled well enough. If it is, then we can solve the problem of polarimetric calibration using ZL. If not, then we can seek *self-calibration* of some parameters.

4. Thermal emission is unpolarized, hence does not affect $L_{\kappa}^{\text{Q}}(\mathbf{X}, \lambda)$.

This work is licensed under a Creative Commons Attribution 4.0 License. For more information, see https://creativecommons.org/licenses/by/4.0/

This article has been accepted for publication in IEEE Transactions on Pattern Analysis and Machine Intelligence. This is the author's version which has not been fully edited and content may change prior to final publication. Citation information: DOI 10.1109/TPAMI.2023.3299526

5.1 Polarimetric Calibration

A known ZL scene $\mathcal{S}$ is observed by a camera. Polarization signals depend on the axial orientation of the camera relative to the scene, so it is beneficial to sample a set of orientations. Moreover, a set of multiple measurements helps to suppress the consequence of random measurement noise and random inaccuracies in $\mathcal{S}$. Rotating the instrument around a LOS $\mathcal{L}$ yields different values of $\alpha^{\rm cam}$, which through Eq. (16) alters the signal filtered by the camera optics and the sensor-mounted polarizers at $\mathbf{x}(\mathcal{L})$. A general 3D rotation (see Sec. 3.1) varies $\mathbf{G}_{\rm cam}$, thus the LOSs that correspond to $\mathbf{x}$. Then, pixel $\mathbf{x}$ observes a different part of the known $\mathcal{S}$, diversifying the measurements.

The locations of observable stars and planets are known and saved in a look-up table. Matching these observed points with the look-up table determines orientation, using onboard star trackers [23]. Star trackers are not always mounted in nano-satellites, due to resource limitations. Nevertheless, we do not need a star-tracker to sense $\mathbf{G}_{\rm cam}$, because, by definition, we have an observational camera that happens to sense these point sources, along with ZL. Hence $\mathbf{G}_{\rm cam}$ is determined from the image data. Noisy measurements at $\mathbf{x}$ constitute a column vector $\boldsymbol{n}_k^{\rm measure}(\mathbf{x})$. Define a fitting error

$$E(\Psi_{\mathbf{x}}, \mathcal{S}) = \sum_{\mathbf{x}} \sum_{k=1}^{K} |\boldsymbol{n}_k^{\rm measure}(\mathbf{x}) - \bar{\boldsymbol{n}}(\mathbf{x}, \Psi_{\mathbf{x}}, \mathcal{S}, \mathbf{G}_{\rm cam})|^2 \ . \tag{33}$$

The sum over $\mathbf{x}$ excludes pixels corresponding to planets and observable stars, known from the 2MASS catalog. Then, assuming $\mathcal{S}$ is modeled and known, calibration is performed by solving the optimization problem

$$\hat{\Psi}_{\mathbf{x}} = \underset{\Psi_{\mathbf{x}}}{\rm argmin}\ E(\Psi_{\mathbf{x}}, \mathcal{S}) \ . \tag{34}$$

Note that the entire forward model is differentiable. Moreover, there are some parameters for which the forward model is linear. Hence, optimization can be done efficiently.

We estimate $\Psi_{\mathbf{x}}$ per camera pixel $\mathbf{x}$ using alternating minimization. We initialize $P, \mathbf{B}$ using corresponding values $P^{\rm prev}, \mathbf{B}^{\rm prev}$ from a previous calibration, done for example pre-launch in a lab, or from previous spaceborne sessions. Then, we iterate two steps: $\{1\}$ Estimate P assuming $\mathbf{B}$ and $\mathcal{S}$ are known; $\{2\}$ Estimate $\mathbf{B}$ assuming P and $\mathcal{S}$ are known.

Define the $4K \times 1$ column-stacked data vector

$$\mathbf{N}^{\rm measure} = \left[(\boldsymbol{n}_1^{\rm measure})^\top ,\ (\boldsymbol{n}_2^{\rm measure})^\top \ \ldots \ (\boldsymbol{n}_K^{\rm measure})^\top \right]^\top . \tag{35}$$

Define the Stokes vector that arrives at the pixel polarizers after the camera optics,

$$\tilde{\boldsymbol{s}}_k^P \equiv \begin{bmatrix} \tilde{I}_k^P \\ \tilde{Q}_k^P \\ \tilde{U}_k^P \end{bmatrix} = \mathbf{B}\mathbf{R}_k \tilde{\boldsymbol{s}}_k \ . \tag{36}$$

The matrix $\mathbf{B}$ is assumed to be known in step $\{1\}$. So, define known column vectors of length $4K$,

$$\mathbf{S}_P = \frac{1}{2} \left[\tilde{Q}_1^P, \tilde{U}_1^P, -\tilde{Q}_1^P, -\tilde{U}_1^P \ \ldots \ \tilde{Q}_K^P, \tilde{U}_K^P, -\tilde{Q}_K^P, -\tilde{U}_K^P \right]^\top . \tag{37}$$

$$\mathbf{I}_P = \left[\tilde{I}_1^P, \tilde{I}_1^P, \tilde{I}_1^P, \tilde{I}_1^P \ \ldots \ \tilde{I}_K^P, \tilde{I}_K^P, \tilde{I}_K^P, \tilde{I}_K^P \right]^\top . \tag{38}$$

From Eqs. (26,33,35,37,38), the forward model is

$$\mathbf{N}^{\rm measure} = \frac{1}{2}\mathbf{I}_P + \mathbf{S}_P P \ . \tag{39}$$

Because $\mathbf{S}_P$ stems from independent measurements, we use a pseudo-inverse

$$\hat{P} = \left(\mathbf{S}_P^\top \mathbf{S}_P \right)^{-1} \mathbf{S}_P^\top (\mathbf{N}^{\rm measure} - \mathbf{I}_P/2) \ . \tag{40}$$

The elements of $\tilde{\boldsymbol{s}}_k = [\tilde{I}_k, \tilde{Q}_k, \tilde{U}_k]^\top$ defined in Eq. (25) are known here. Then, step $\{2\}$ estimates $\mathtt{a}, \mathtt{b}, \mathtt{c}$ as follows. Define the known terms

$$\mathtt{g}_k = \tilde{Q}_k \cos 2\alpha_k^{\rm cam} - \tilde{U}_k \sin 2\alpha_k^{\rm cam} \ , \tag{41}$$

$$\mathtt{f}_k = \tilde{Q}_k \sin 2\alpha_k^{\rm cam} + \tilde{U}_k \cos 2\alpha_k^{\rm cam} \ . \tag{42}$$

Define a known $4K \times 3$ matrix $\mathbf{F}_B$ and a $4K \times 1$ vector $\mathbf{I}_B$:

$$\mathbf{F}_B = \frac{P}{2} \begin{bmatrix} \mathtt{g}_1 & 0 & -\mathtt{g}_1 & 0 & \ldots & -\mathtt{g}_K & 0 \\ \mathtt{f}_1 & \mathtt{g}_1 & -\mathtt{f}_1 & -\mathtt{g}_1 & \ldots & -\mathtt{f}_K & -\mathtt{g}_K \\ 0 & \mathtt{f}_1 & 0 & -\mathtt{f}_1 & \ldots & 0 & -\mathtt{f}_K \end{bmatrix}^\top , \tag{43}$$

$$\mathbf{I}_B = \left[\tilde{I}_1, \tilde{I}_1, \tilde{I}_1, \tilde{I}_1 \ \ldots \ \tilde{I}_K, \tilde{I}_K, \tilde{I}_K, \tilde{I}_K \ \right]^\top . \tag{44}$$

From Eqs. (19,26,33,35,43,44)

$$\mathbf{N}^{\rm measure} = \frac{1}{2}\mathbf{I}_B + \mathbf{F}_B \left[\mathtt{a}\ \mathtt{b}\ \mathtt{c} \right]^\top \ . \tag{45}$$

Then, pseudo-inverse yields

$$\begin{bmatrix} \hat{\mathtt{a}} \\ \hat{\mathtt{b}} \\ \hat{\mathtt{c}} \end{bmatrix} = \left(\mathbf{F}_B^\top \mathbf{F}_B \right)^{-1} \mathbf{F}_B^\top (\mathbf{N}^{\rm measure} - \mathbf{I}_B/2) \ . \tag{46}$$

In typical optical systems, birefringence is generally a smooth function, thus changing slowly across the field of view. Therefore, we smooth the pixel-based results $\hat{\mathtt{a}}, \hat{\mathtt{b}}, \hat{\mathtt{c}}$. We use a spatial mean having a support of 5×5 superpixels.

5.2 Polarimetric Self-Calibration

Current ZL models are not yet good enough for calibration. We then suggest self-calibration, motivated by [25]. Here, a camera observes an unknown scene $\mathcal{S}$. We need to solve

$$\hat{\Psi}_{\mathbf{x}}, \hat{\mathcal{S}} = \underset{\Psi_{\mathbf{x}}, \mathcal{S}}{\rm argmin}\ E(\Psi_{\mathbf{x}}, \mathcal{S}) \ . \tag{47}$$

The polarizance P of the imager pixels changes slowly in time. Birefringence, on the other hand, is a fast effect, caused by thermal variations in a harsh environment. At the beginning of a mission, the effects of $\mathbf{B}$ can be studied, assuming P is as measured in the lab. Over time, P can be re-estimated as well. We assume that over the entire camera, some of the pixels are not degraded since a prior measurement. They can anchor P.

We generalize Sec. 5.1, by iterating three steps:
(i) Estimate $\mathcal{S}$ assuming P and $\mathbf{B}$ are known. Initially, we use $P^{\rm prev}$ and $\mathbf{B}^{\rm prev}$.
(ii) Estimate P assuming $\mathbf{B}$ and $\mathcal{S}$ are known.
(iii) Estimate $\mathbf{B}$ assuming P and $\mathcal{S}$ are known.
We iterate until convergence. Steps (ii) and (iii) are the same as described in Sec. 5.1. In this section, we describe step (i).

The estimate of the Stokes vector of LOS $\mathcal{L}$ is $\tilde{\boldsymbol{s}}_{\mathcal{L}}$. This LOS is sequentially projected to a set of superpixels

This work is licensed under a Creative Commons Attribution 4.0 License. For more information, see https://creativecommons.org/licenses/by/4.0/

This article has been accepted for publication in IEEE Transactions on Pattern Analysis and Machine Intelligence. This is the author's version which has not been fully edited and content may change prior to final publication. Citation information: DOI 10.1109/TPAMI.2023.3299526

$\{\mathbf{x}_k\}_{k=1}^K$. We align the images using stars and planets, and then associate $\mathcal{L}$ to superpixels by nearest-neighbor interpolation. When $\mathcal{L}$ is projected to $\mathbf{x}_k$, the measured numbers of electrons are represented by the 4×1 vector

$$\mathbf{n}_{\mathcal{L},k}^{\text{measure}} = \left[N_{\mathcal{L},k}^{\text{measure}}(0^\circ) \ \ldots \ N_{\mathcal{L},k}^{\text{measure}}(135^\circ)\right]^\top . \tag{48}$$

Let $\mathbf{n}_{\mathcal{L}}^{\text{measure}}$ be the $4K \times 1$ vector of measurements corresponding to $\mathcal{L}$, measured at $\{\mathbf{x}_k\}_{k=1}^K$:

$$\mathbf{n}_{\mathcal{L}}^{\text{measure}} = \left[\left(\mathbf{n}_{\mathcal{L},1}^{\text{measure}}\right)^\top \ldots \ \left(\mathbf{n}_{\mathcal{L},K}^{\text{measure}}\right)^\top\right]^\top . \tag{49}$$

Each super-pixel $\mathbf{x}_k$ has a different set $\Psi_{\mathbf{x}}$, thus corresponding matrices $\mathbf{V}_{\mathbf{x}_k}, \mathbf{B}_{\mathbf{x}_k}$. Let $\mathbf{0}_{\mathtt{n}\times\mathtt{m}}$ be an $\mathtt{n} \times \mathtt{m}$ zero matrix. Using Eq. (19), define the matrices

$$\tilde{\mathbf{V}}_{\mathcal{L}} = \begin{bmatrix} \mathbf{V}_{\mathbf{x}_1} & \mathbf{0}_{4\times3} & \ldots & \mathbf{0}_{4\times3} \\ \mathbf{0}_{4\times3} & \mathbf{V}_{\mathbf{x}_2} & \ldots & \mathbf{0}_{4\times3} \\ \vdots & \vdots & & \vdots \\ \mathbf{0}_{4\times3} & \mathbf{0}_{4\times3} & \ldots & \mathbf{V}_{\mathbf{x}_K} \end{bmatrix}_{4K\times3K} , \tag{50}$$

$$\tilde{\mathbf{B}}_{\mathcal{L}} = \begin{bmatrix} \mathbf{B}_{\mathbf{x}_1} & \mathbf{0}_{3\times3} & \ldots & \mathbf{0}_{3\times3} \\ \mathbf{0}_{3\times3} & \mathbf{B}_{\mathbf{x}_2} & \ldots & \mathbf{0}_{3\times3} \\ \vdots & \vdots & & \vdots \\ \mathbf{0}_{3\times3} & \mathbf{0}_{3\times3} & \ldots & \mathbf{B}_{\mathbf{x}_K} \end{bmatrix}_{3K\times3K} . \tag{51}$$

Using the corresponding rotation Muller matrices $\{\mathbf{R}_k\}_{k=1}^K$, define the $3K \times 3$ matrix

$$\tilde{\mathbf{R}} = \left[\mathbf{R}_1^\top, \mathbf{R}_2^\top \ \ldots \ \mathbf{R}_K^\top\right]^\top . \tag{52}$$

From Eqs. (26,49,50,51,52),

$$\mathbf{n}_{\mathcal{L}}^{\text{measure}} = \tilde{\mathbf{V}}_{\mathcal{L}}\tilde{\mathbf{B}}_{\mathcal{L}}\tilde{\mathbf{R}}\tilde{\boldsymbol{s}}_{\mathcal{L}} \equiv \mathbf{F}_s\tilde{\boldsymbol{s}}_{\mathcal{L}} , \tag{53}$$

where $\mathbf{F}_s = \tilde{\mathbf{V}}_{\mathcal{L}}\tilde{\mathbf{B}}_{\mathcal{L}}\tilde{\mathbf{R}}$. Using a pseudo-inverse of Eq. (53),

$$\hat{\boldsymbol{s}}_{\mathcal{L}} = \left(\mathbf{F}_s^\top\mathbf{F}_s\right)^{-1}\mathbf{F}_s^\top\mathbf{n}_{\mathcal{L}}^{\text{measure}} . \tag{54}$$

5.3 Constraints

Pseudo-inverse steps do not impose natural constraints on the variables. Moreover, there is an ambiguity that needs to be resolved. These matters are handled in this section.

5.3.1 Birefringence

Recall the form of matrix $\mathbf{B}$ from Eqs. (10,11,15). Define the matrices

$$\mathbf{M}_{QU} = \begin{bmatrix} 1 & 0 \\ 0 & \cos\delta \end{bmatrix}, \ \ \mathbf{R}_{QU} = \begin{bmatrix} \cos(2\alpha_{\text{br}}) & \sin(2\alpha_{\text{br}}) \\ -\sin(2\alpha_{\text{br}}) & \cos(2\alpha_{\text{br}}) \end{bmatrix}. \tag{55}$$

Then,

$$\mathbf{B}_{QU} \equiv \begin{bmatrix} \mathtt{a} & \mathtt{b} \\ \mathtt{b} & \mathtt{c} \end{bmatrix} = \mathbf{R}_{QU}^{-1}\mathbf{M}_{QU}\mathbf{R}_{QU} . \tag{56}$$

Consequently, the eigenvalues of $\mathbf{B}_{QU}$ must be $\{1, \cos\delta\}$. This is a constraint. Section 5.1 yields $\hat{\mathtt{a}}, \hat{\mathtt{b}}, \hat{\mathtt{c}}$. These values form a matrix that is diagonalized as follows:

$$\hat{\mathbf{B}}_{QU} = \begin{bmatrix} \hat{\mathtt{a}} & \hat{\mathtt{b}} \\ \hat{\mathtt{b}} & \hat{\mathtt{c}} \end{bmatrix} = \mathbf{J}^\top \begin{bmatrix} \mathtt{e}_1 & 0 \\ 0 & \mathtt{e}_2 \end{bmatrix} \mathbf{J} . \tag{57}$$

Here $\mathbf{J}$ is a rotation matrix made of orthonormal eigenvectors, while $\{\mathtt{e}_1, \mathtt{e}_2\}$ are the eigenvalues of $\hat{\mathbf{B}}_{QU}$. The matrix

$$\hat{\mathbf{B}}'_{QU} = \mathbf{J}^\top \begin{bmatrix} \mathtt{e}_1/\max(\mathtt{e}_1, \mathtt{e}_2) & 0 \\ 0 & \mathtt{e}_2/\max(\mathtt{e}_1, \mathtt{e}_2) \end{bmatrix} \mathbf{J} \tag{58}$$

satisfies the eigenvalue constraint. Based on $\hat{\mathbf{B}}'_{QU}$, the constrained values of $\hat{\mathtt{a}}, \hat{\mathtt{b}}, \hat{\mathtt{c}}$ are extracted, in matrix elements corresponding to Eqs. (56,57). This is done in each iteration.

5.3.2 Polarizance

Because $0 \le P(\mathbf{x}) \le 1$, then $\hat{P}(\mathbf{x})$ is clipped to this range in each iteration. Still, self-calibration has an inherent ambiguity, as the scene is unknown. Consider Eqs. (8,9,10,11,16,17). Suppose we scale the polarization components of the scene by a factor ξ, such that $Q_{\mathcal{L}}(\lambda) \to \xi Q_{\mathcal{L}}(\lambda)$ and $U_{\mathcal{L}}(\lambda) \to \xi U_{\mathcal{L}}(\lambda)$. Simultaneously, suppose that the polarizance is scaled as $P \to P/\xi$. Then, the measurement I_{cam} in Eq. (17) is invariant to this scale. Hence, when using only polarimetric data without a prior, there is a fundamental scale ambiguity in estimating P.

Our disambiguation uses two priors: {i} Over time, the polarizance $P(\mathbf{x})$ is monotonically not-increasing. {ii} Pixels degrade at different rates. Some pixels are least degraded: their polarizance is very close, or equal to the corresponding value $\hat{P}^{\text{prev}}(\mathbf{x})$ measured previously (prelaunch in the lab, or in a previous spaceborne calibration).

Consequently, define $\chi(\mathbf{x}) = [\hat{P}(\mathbf{x})/\hat{P}^{\text{prev}}(\mathbf{x})]$. Consider a re-scaled polarizance $\hat{P}'(\mathbf{x}) = \hat{P}(\mathbf{x})[\max_{\mathbf{x}} \chi(\mathbf{x})]^{-1}$. The map $\hat{P}'(\mathbf{x})$ is resistant to scale ambiguity. The least-degraded pixel yields $\hat{P}'(\mathbf{x}) = \hat{P}^{\text{prev}}(\mathbf{x})$, correctly when intact. However, a maximum is not robust to noise. Hence, sort $\chi(\mathbf{x})$. Let $\mathbf{x}_{95\%}$ be the pixel corresponding to the 95^{th} percentile of $\chi(\mathbf{x})$. We then use $\hat{P}'(\mathbf{x}) = \hat{P}(\mathbf{x})[\chi(\mathbf{x}_{95\%})]^{-1}$.

6 Simulation

We simulated observations of ZL as in Sec. 4. The simulated imager field of view spans 5°, having a resolution of 200×300 pixels. The imager parameters are set to $p^2 = (7\mu m)^2$, $D = 16.6mm$, $f = 24mm$, $\tau_\lambda = 0.96$, a red spectral band, $100nm$ wide and $\text{QE}_\lambda \approx 0.8$. The imager has spatially varying ground-truth polarization parameters $\Psi_{\mathbf{x}}^{\text{true}}$. Spatial maps of the corresponding ground-truth P^{true}, $\mathtt{a}^{\text{true}}$, $\mathtt{b}^{\text{true}}$, $\mathtt{c}^{\text{true}}$ appear in Fig. 12.

The simulation was done for June 14th, 2022. As a baseline (which we deviate from), the imager is directed 17° away from the sun, on the ecliptic plane, 65° from the vernal equinox. An example of simulated image data is shown in Fig. 13. Based on ZL characteristics and specifications of the simulated camera, we calculated the expected signals. As a baseline (which we deviate from in an ablation study), we use exposure time $\Delta t = 10s$ and $K = 30$ measurements, each at a different camera orientation. To achieve a signal in the range of thousands of photoelectrons, a long exposure time of around $\Delta t = 10s$ is required in this system. This induces significant dark noise. To reduce noise variance, in each measurement k, we capture 20 images (in 3.3 minutes) and temporally average them. ZL and the background remain effectively static during this time.

6.1 Simulation Noise

The actual measured number of electrons is random due to noise. Photoelectrons are Poisson distributed as

$$\tilde{N}(\mathbf{x}) \sim \text{Poisson}[\bar{N}(\mathbf{x})] . \tag{59}$$

This work is licensed under a Creative Commons Attribution 4.0 License. For more information, see https://creativecommons.org/licenses/by/4.0/

This article has been accepted for publication in IEEE Transactions on Pattern Analysis and Machine Intelligence. This is the author's version which has not been fully edited and content may change prior to final publication. Citation information: DOI 10.1109/TPAMI.2023.3299526

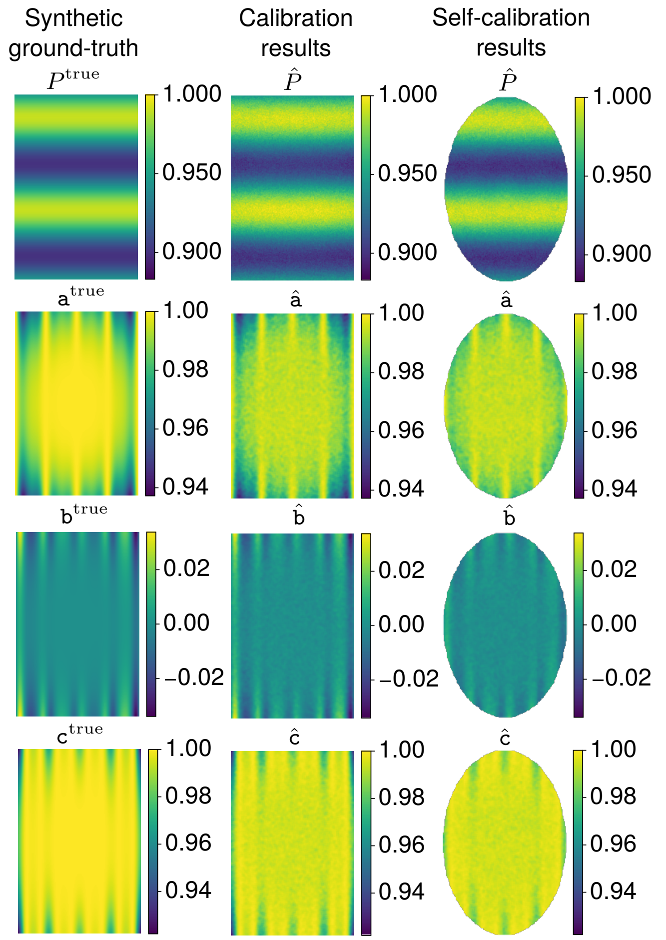

Fig. 12. (Left) Synthetic ground-truth spatial maps P^{true}, a^{true}, b^{true}, c^{true}. (Center) Calibrated maps. (Right) Self-calibrated maps.

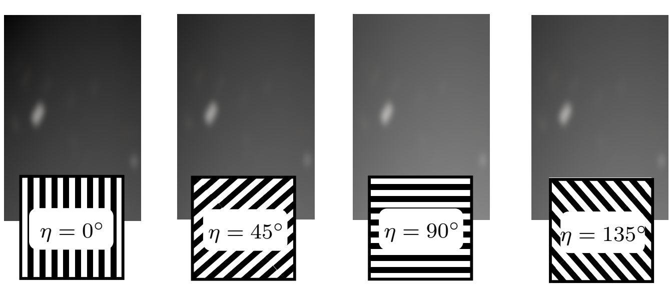

Fig. 13. Simulated sky images (per polarizer angle angle η), including ZL and background stars. Simulated for June 14th, 2022, directed $37°$ away from the sun, on the ecliptic plane, $45°$ from the vernal equinox. For display clarity only, the images are presented gamma corrected with $\gamma = 0.6$.

A camera has dark current $\mathcal{B}_T$ (in units of electrons per second), which depends on the sensor temperature T. It yields dark noise $\zeta_{\text{dark}} \sim \mathcal{N}(\mathcal{B}_T\Delta t, \mathcal{B}_T\Delta t)$. The readout electronics have read-noise $\zeta_{\text{read}} \sim \mathcal{N}\left(0, \sigma^2_{\text{read}}\right)$ having a standard deviation of σ_{read} electrons. A pixel full well has N_{full} electrons. The measurement is quantized by b bits. So, a model [50] for a noisy measurement of photo-electrons is

$$\tilde{N}^{\text{measured}}(\mathbf{x}) = \frac{N_{\text{full}}}{2^b}\left\lfloor \frac{2^b}{N_{\text{full}}}\left\{\tilde{N}(\mathbf{x}) + \zeta_{\text{read}} + \zeta_{\text{dark}}\right\}\right\rfloor . \tag{60}$$

Values of $\tilde{N}^{\text{measured}}$ higher than N_{full} are clipped. The simulation uses noise parameters $\mathcal{B}_T = 3.51s^{-1}$, $\sigma_{\text{read}} = 2.31$, $N_{\text{full}} = 10500$, and $b = 10$.

Camera jitter causes a random motion path, averaged during the exposure time. We set a jitter [23] amplitude $\sim 0.1°$. Based on the camera specifications above, this corresponds to blur by a Gaussian kernel having a standard deviation of 4 pixels, and blur by rotation around the optical axis (RAOA). Blur by RAOA is simulated by a weighted sum of rotated images, each indexed i and rotated by angle α_i. Geometric rotation maps to $\mathbf{x}$ a pixel $\mathbf{x}_i = \mathbf{G}_{\alpha_i}\mathbf{x}$, where $\mathbf{G}_{\alpha_i}$ is a rotation matrix in the image plane. As in Eq. (23), this mapping leads $\mathbf{x}$ to sense light along a projected LOS $\mathcal{L}(i) \rightarrow \mathbf{x}_i$. RAOA also rotates the Stokes vector. This perturbation is defined by a Muller rotation matrix $\mathbf{R}_{\alpha_i}$. Combining these two RAOA effects, a Stokes vector that is axially rotated and averaged during Δt is simulated by

$$\boldsymbol{s}^{\text{blur}}_{\mathbf{x}} = \sum_i w_i \mathbf{R}_{\alpha_i} \boldsymbol{s}\{\mathcal{L}(i) \rightarrow \mathbf{x}_i\} , \tag{61}$$

using the weight $w_i \sim \exp(-[\alpha_i/0.1°]^2/2)$. A sensitivity study we performed shows that jitter having a directional amplitude of up to $0.2°$ does not affect the results.

6.2 Simulation results

In pre-processing, we remove the bias caused by dark noise, $N^{\text{measured}} = \tilde{N}^{\text{measured}} - \mathcal{B}_T\Delta t$. We assume that calibration is done occasionally during the mission lifetime, so we have rough previous estimates $\hat{P}^{\text{prev}}, \hat{\mathbf{B}}^{\text{prev}}$ that need to be refined. These values thus initialize the optimization, and are likely not far from the true values. Hence, we set the initial values as noisy versions of the ground truth. Let $z_P \sim \mathcal{N}(0.02, 0.01^2)$ and $z_{\mathsf{a}}, z_{\mathsf{b}}, z_{\mathsf{c}} \sim \mathcal{N}(0, 0.02^2)$. Then, we set $\hat{P}^{\text{prev}} = P^{\text{true}} + z_P$, $\hat{\mathsf{a}}^{\text{prev}} = \mathsf{a}^{\text{true}} + z_{\mathsf{a}}$, $\hat{\mathsf{b}}^{\text{prev}} = \mathsf{b}^{\text{true}} + z_{\mathsf{b}}$, $\hat{\mathsf{c}}^{\text{prev}} = \mathsf{c}^{\text{true}} + z_{\mathsf{c}}$ and clip the values to the valid domains of P and $\mathbf{B}$. The matrix $\hat{\mathbf{B}}^{\text{prev}}$ is formed based on Eq. (15) using $\hat{\mathsf{a}}^{\text{prev}}, \hat{\mathsf{b}}^{\text{prev}}, \hat{\mathsf{c}}^{\text{prev}}$.

We quantify results using root mean squared errors (RMSE). Let $\|\cdot\|_2^{\frac{1}{2}}$ and $\|\cdot\|_F^{\frac{1}{2}}$ be respectively the ℓ_2 norm and Frobenius norm of arrays. Here the arrays span estimations at all pixels $\mathbf{x}$ and sampled examples. Then,

$$\text{RMSE}(P) = \|P^{\text{true}}(\mathbf{x}) - \hat{P}(\mathbf{x})\|_2^{\frac{1}{2}} . \tag{62}$$

$$\text{RMSE}(\mathbf{B}) = \|\mathbf{B}^{\text{true}}(\mathbf{x}) - \hat{\mathbf{B}}(\mathbf{x})\|_F^{\frac{1}{2}} . \tag{63}$$

Prior to calibration, $\text{RMSE}(P) \approx 2\%$ and $\text{RMSE}(\mathbf{B}) \approx 2\%$. Calibration optimization converges within 3-4 iterations. After convergence, calibration reached $\text{RMSE}(P) \approx 0.6\%$ and $\text{MSE}(\mathbf{B}) \approx 0.3\%$. Results are shown in Fig. 12.

In self-calibration, observations were taken by rotating the camera around its axis. So, self-calibration estimations are valid in pixels within an ellipse around the center of the sensor array. Within the ellipse, all pixels are exposed in all measurements. Self-calibration achieved $\text{RMSE}(P) \approx 0.5\%$ and $\text{RMSE}(\mathbf{B}) \approx 0.3\%$. Self-calibration results are shown in Fig. 12. Calibration and self-calibration results are assessed in scatter plots (Fig. 14).

Sec. 5.1 mentions spatial smoothing of $\hat{\mathsf{a}}, \hat{\mathsf{b}}, \hat{\mathsf{c}}$ after each iteration. We made an ablation test. Introducing smoothing by kernels of sizes 3×3, 5×5 and 9×9 improve $\text{RMSE}(\mathbf{B})$ by $\times1.3$, $\times2$, $\times2$, respectively. So, we settle for a 5×5 kernel.

This work is licensed under a Creative Commons Attribution 4.0 License. For more information, see https://creativecommons.org/licenses/by/4.0/

This article has been accepted for publication in IEEE Transactions on Pattern Analysis and Machine Intelligence. This is the author's version which has not been fully edited and content may change prior to final publication. Citation information: DOI 10.1109/TPAMI.2023.3299526

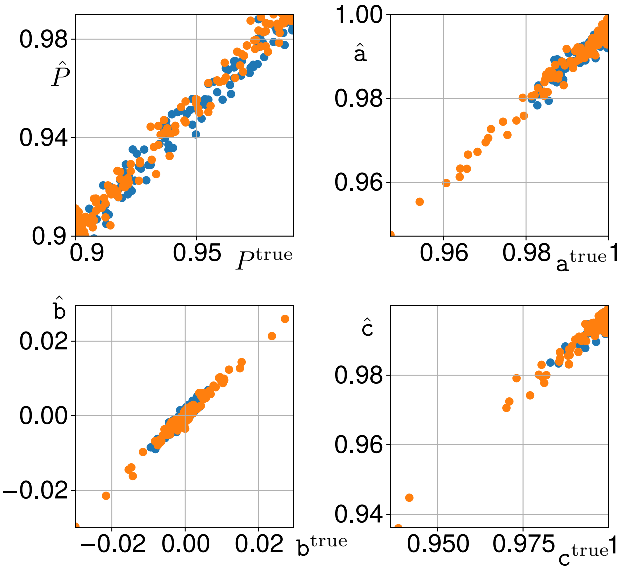

Fig. 14. Scatter plots of simulated calibrated (orange) and self-calibrated (blue) $P, \mathtt{a}, \mathtt{b}, \mathtt{c}$ results. Here $\Delta t = 10s$ and $K = 30$. Displayed points are 150 randomly sampled representative super-pixels out of the total array.

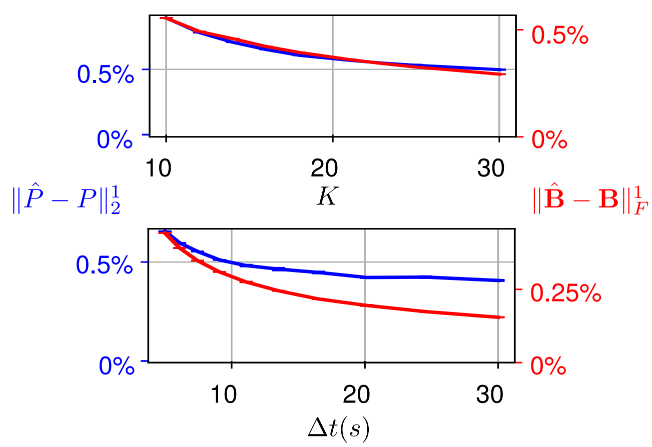

Fig. 15. Self-calibration $\mathrm{RMSE}(P)$ and $\mathrm{RMSE}(\mathbf{B})$ as a function of K with $\Delta t = 10s$ [Top], and as a function of Δt with $K = 30$ [Bottom]. Fifteen simulations were done, to assess RMSE mean and standard deviation. Without self-calibration, P and $\mathbf{B}$ have RMSE of 2%.

An ablation study tests the effects of K and Δt. One test uses $K = 30$. Then, increasing Δt from 5s to 30s, improves the final calibration $\mathrm{RMSE}(P)$ and $\mathrm{RMSE}(\mathbf{B})$ by $\times 1.6$ and $\times 2.8$, respectively. Another test uses $\Delta t = 10s$. Then, increasing K from 10 to 30, improves the final calibration $\mathrm{RMSE}(P)$ and $\mathrm{RMSE}(\mathbf{B})$ by $\times 1.8$ and $\times 1.9$ respectively. Such trends also appear in tests of self-calibration, as shown in Fig. 15. From this figure, the product $K\Delta t$ is 5 minutes. Since we averaged 20 images per observation, this means $\approx 1.6\mathrm{hours}$ total acquisition time. Increasing the acquisition time improves the results.

The acquisition time relates to D and the intensity of ZL. Recall that the baseline test points $17°$ away from the sun. To avoid lens-flare [67], [68], however, such an angle requires the sun to be eclipsed. This can be achieved by being at Earth's night side while the sun is $17°$ beyond the horizon. This limits the timing of calibration sessions. Directions farther from the sun have lower ZL radiance. So, to achieve similar signals, directing the imager $27°$ or $37°$ away from the sun requires, respectively, $\Delta t = 30\mathrm{s}$ and $\Delta t = 60\mathrm{s}$. The long acquisition time stems from the noise parameters listed in Sec. 6.1. Larger optics (D) or lower $\mathcal{B}_T$ can yield a high signal-to-noise ratio using shorter Δt and fewer images.

7 Discussion

Computational imaging contributes to astrophysics, as evident by [69]. We suggest spaceborne polarimetric camera calibration and self-calibration using ZL. This principle exploits a natural phenomenon that occurs at a relatively large distance at a wide angle. There is wide tolerance to pose deviations. A natural phenomenon does not require using special equipment onboard or outside a spacecraft. ZL changes very slowly and is relatively predictable.

The approach is not limited to LEO. We believe it can also be helpful for deep space probes, observing ZL, or other reliable polarized sources. Future research should hopefully demonstrate these methods using spaceborne data taken by future missions. The paper already includes many sources of disturbances: spatially varying birefringence and polarizance, integrated starlight, thermal and photon noise, motion blur, and rotational perturbation to the Mueller matrix by platform jitter. Real measurements may be affected by additional sources. Further real-world discrepancies, so far unaccounted for, can be due to the entry of a comet into the inner solar system, which adds IDPs in its path. New comets are tracked. Thus, during calibration, the imager can point to a sky region that has no overlap with a new comet's path.

The optimization can explicitly include a prior of spatial regularity (smoothness) of $\Psi_{\mathbf{x}}$. Thus far, computations of calibration or self-calibration are fast. It takes us less than a minute on a common laptop to perform 10 alternating iterations. The process is expected to be offline, once in a while during a space mission's lifetime. So, the time and computation resources needed are small.

Acknowledgments

We thank Vadim Holodovsky and Roi Ronen for their support. Yoav Schechner is the Mark and Diane Seiden Chair in Science at the Technion. He is a Landau Fellow supported by the Taub Foundation. His work was conducted in the Ollendorff Minerva Center. Minvera is funded through the BMBF. This project has received funding from the European Research Council (ERC) under the European Union's Horizon 2020 research and innovation programme (CloudCT, grant agreement No. 810370). Ehud Behar was supported in part by a Center of Excellence of the Israel Science Foundation (grant No. 1937/19).

References

[1] B. Ghanekar, V. Saragadam, D. Mehra, A.-K. Gustavsson, A. C. Sankaranarayanan, and A. Veeraraghavan, "PS2F: Polarized spiral point spread function for single-shot 3d sensing," *IEEE Transactions on Pattern Analysis and Machine Intelligence*, pp. 1–12, 2022.

[2] T. Maeda, A. Kadambi, Y. Y. Schechner, and R. Raskar, "Dynamic heterodyne interferometry," in *Proc. IEEE International Conference on Computational Photography*, 2018, pp. 1–11.

This work is licensed under a Creative Commons Attribution 4.0 License. For more information, see https://creativecommons.org/licenses/by/4.0/

This article has been accepted for publication in IEEE Transactions on Pattern Analysis and Machine Intelligence. This is the author's version which has not been fully edited and content may change prior to final publication. Citation information: DOI 10.1109/TPAMI.2023.3299526

[3] T. Treibitz and Y. Y. Schechner, "Active polarization descattering," *IEEE Transactions on Pattern Analysis and Machine Intelligence*, vol. 31, no. 3, pp. 385–399, 2008.

[4] N. Karpel and Y. Y. Schechner, "Portable polarimetric underwater imaging system with a linear response," in *Polarization: Measurement, Analysis, and Remote Sensing VI*, vol. 5432. SPIE, 2004, pp. 106–115.

[5] Y. Y. Schechner, D. J. Diner, and J. V. Martonchik, "Spaceborne underwater imaging," in *Proc. IEEE International Conference on Computational Photography*, 2011, pp. 1–8.

[6] R. Horstmeyer, G. Euliss, R. Athale, and M. Levoy, "Flexible multimodal camera using a light field architecture," in *Proc. IEEE International Conference on Computational Photography*, 2009, pp. 1–8.

[7] R. Antonucci and J. Miller, "Spectropolarimetry and the nature of NGC 1068," *The Astrophysical Journal*, vol. 297, pp. 621–632, 1985.

[8] R. A. Laing, "The sidedness of jets and depolarization in powerful extragalactic radio sources," *Nature*, vol. 331, no. 6152, pp. 149–151, 1988.

[9] W. Coburn and S. E. Boggs, "Polarization of the prompt γ-ray emission from the γ-ray burst of 6 December 2002," *Nature*, vol. 423, no. 6938, pp. 415–417, 2003.

[10] H. Krawczynski, F. Muleri, M. Dovčiak, A. Veledina, N. Rodriguez Cavero, J. Svoboda, A. Ingram, G. Matt, J. A. Garcia, V. Loktev *et al.*, "Polarized x-rays constrain the disk-jet geometry in the black hole x-ray binary Cygnus X-1," *Science*, vol. 378, no. 6620, pp. 650–654, 2022.

[11] M. S. Asif, J. Romberg, and R. Baraniuk, "Calibration-free accelerated dynamic MRI based on low-rank matrix recovery," in *Proc. Signal Processing with Adaptive Sparse Structured Representations Workshop*, 2015.

[12] K. N. Kutulakos and J. R. Vallino, "Calibration-free augmented reality," *IEEE Transactions on Visualization and Computer Graphics*, vol. 4, no. 1, pp. 1–20, 1998.

[13] D. S. Weller, J. R. Polimeni, L. Grady, L. L. Wald, E. Adalsteinsson, and V. K. Goyal, "Sparsity-promoting calibration for GRAPPA accelerated parallel MRI reconstruction," *IEEE Transactions on Medical Imaging*, vol. 32, no. 7, pp. 1325–1335, 2013.

[14] M. Sheinin, D. N. Reddy, M. O'Toole, and S. G. Narasimhan, "Diffraction line imaging," in *Proc. European Conference on Computer Vision*, 2020, pp. 1–16.

[15] E. Alexander, Q. Guo, S. Koppal, S. Gortler, and T. Zickler, "Focal flow: Measuring distance and velocity with defocus and differential motion," in *Proc. European Conference on Computer Vision*, 2016, pp. 667–682.

[16] B. Atcheson, F. Heide, and W. Heidrich, "CALTag: High precision fiducial markers for camera calibration." in *Proc. Vision, Modeling, and Visualization*, 2010, pp. 41–48.

[17] Y. Y. Schechner and S. K. Nayar, "Uncontrolled modulation imaging," in *Proc. IEEE Computer Society Conference on Computer Vision and Pattern Recognition*, vol. 2, 2004, pp. II–II.

[18] A. Litvinov and Y. Y. Schechner, "Addressing radiometric nonidealities: A unified framework," in *Proc. IEEE Computer Society Conference on Computer Vision and Pattern Recognition*, vol. 2, 2005, pp. 52–59.

[19] G. Merlin, J. Riedi, L. C. Labonnote, C. Cornet, A. B. Davis, P. Dubuisson, M. Desmons, N. Ferlay, and F. Parol, "Cloud information content analysis of multi-angular measurements in the oxygen A-band: application to 3MI and MSPI," *Atmospheric Measurement Techniques*, vol. 9, no. 10, pp. 4977–4995, 2016.

[20] R. A. Chipman, W. S. T. Lam, and G. Young, *Polarized Light and Optical Systems*. CRC press, 2018.

[21] C. J. Bruegge, D. J. Diner, R. A. Kahn, N. Chrien, M. C. Helmlinger, B. J. Gaitley, and W. A. Abdou, "The MISR radiometric calibration process," *Remote Sensing of Environment*, vol. 107, no. 1-2, pp. 2–11, 2007.

[22] J. L. Pezzaniti and D. B. Chenault, "A division of aperture MWIR imaging polarimeter," in *Polarization Science and Remote Sensing II*, vol. 5888. SPIE, 2005, pp. 239–250.

[23] G. Sebestyen, S. Fujikawa, N. Galassi, and A. Chuchra, *Low Earth Orbit Satellite Design*. Springer, 2018, p. 99.

[24] Y. Beletsky, "Zodiacal light over La Silla," 2014, licensed under CC 4.0. [Online]. Available: https://www.eso.org/public/images/zodiacal_beletsky_potw/#:~:text=A%20sea%20of%20clouds%20has,close%20to%20sunrise%20or%20sunset.

[25] Y. Y. Schechner, "Self-calibrating imaging polarimetry," in *Proc. IEEE International Conference on Computational Photography*, 2015, pp. 1–10.

[26] M. Tzabari and Y. Y. Schechner, "Polarized optical-flow gyroscope," in *Proc. European Conference On Computer Vision*. Springer, 2020, pp. 363–381.

[27] S. Zane, B. Winter, C. Theobalds, T. Theodorou, M. Pinchera, F. Muleri, F. Spada, C. Sgro, D. Zanetti, H. Feng *et al.*, "The on-board calibration system of the X-ray imaging polarimetry explorer (XIPE)," in *Proc. Space Telescopes and Instrumentation*, vol. 9905. SPIE, 2016, pp. 1408–1422.

[28] M. Liu, X. Zhang, T. Liu, G. Shi, L. Wang, and Y. Li, "On-orbit polarization calibration for multichannel polarimetric camera," *Applied Sciences*, vol. 9, no. 7, p. 1424, 2019.

[29] J. Guo, Z. Yao, Z. Han, Z. Zhao, J. Jiang, and W. Yan, "On-orbit polarization calibration of the multi-angle polarization imager based on sunglint over the ocean," in *Proc. of the Tiangong-2 Remote Sensing Application Conference: Technology, Method and Application*. Springer, 2019, pp. 144–159.

[30] S. Zhu, Z. Li, L. Qie, H. Xu, B. Ge, Y. Xie, R. Qiao, Y. Xie, J. Hong, B. Meng *et al.*, "In-flight relative radiometric calibration of a wide field of view directional polarimetric camera based on the rayleigh scattering over ocean," *Remote Sensing*, vol. 14, no. 5, p. 1211, 2022.

[31] L. Qie, Z. Li, S. Zhu, H. Xu, Y. Xie, R. Qiao, J. Hong, and B. Tu, "In-flight radiometric and polarimetric calibration of the directional polarimetric camera onboard the GaoFen-5 satellite over the ocean," *Applied Optics*, vol. 60, no. 24, pp. 7186–7199, 2021.

[32] Y. Bertschy and Y. Y. Schechner, "Vicarious spaceborne polarimetric camera calibration using solar power stations," in *Polarization: Measurement, Analysis, and Remote Sensing XV*, vol. 12112. SPIE, 2022, pp. 132–142.

[33] F. J. Casas, E. Martínez-González, J. Bermejo-Ballesteros, S. García, J. Cubas, P. Vielva, R. B. Barreiro, and A. Sanz, "L2-CalSat: A calibration satellite for ultra-sensitive CMB polarization space missions," *Sensors*, vol. 21, no. 10, p. 3361, 2021.

[34] M. Tzabari, V. Holodovsky, O. Shubi, E. Eytan, O. Altaratz, I. Koren, A. Aumann, K. Schilling, and Y. Y. Schechner, "CloudCT 3D volumetric tomography: considerations for imager preference, comparing visible light, short-wave infrared, and polarized imagers," in *Polarization Science and Remote Sensing X*, vol. 11833. SPIE, 2021, pp. 19–26.

[35] D. J. Diner, S. W. Boland, M. Brauer, C. Bruegge, K. A. Burke, R. Chipman, L. Di Girolamo, M. J. Garay, S. Hasheminassab, E. Hyer *et al.*, "Advances in multiangle satellite remote sensing of speciated airborne particulate matter and association with adverse health effects: from MISR to MAIA," *Journal of Applied Remote Sensing*, vol. 12, no. 4, p. 042603, 2018.

[36] R. Fernandez Borda, J. Martins, B. McBride, L. Remer, and H. Barbosa, "Capabilities of the HARP2 polarimetric sensor on the PACE satellite," in *Proc. AGU Fall Meeting*, 2018, pp. OS11D–1431.

[37] J. Lasue, A.-C. Levasseur-Regourd, and J.-B. Renard, "Zodiacal light observations and its link with cosmic dust: A review," *Planetary and Space Science*, vol. 190, p. 104973, 2020.

[38] G. Neugebauer, H. Habing, R. Van Duinen, H. Aumann, B. Baud, C. Beichman, D. Beintema, N. Boggess, P. Clegg, T. De Jong *et al.*, "The infrared astronomical satellite (IRAS) mission," *The Astrophysical Journal*, vol. 278, pp. L1–L6, 1984.

[39] J. C. Mather, "The cosmic background explorer (COBE)," *Optical Engineering*, vol. 21, no. 4, pp. 769–774, 1982.

[40] M. Kessler, J. Steinz, M. Anderegg, J. Clavel, G. Drechsel, P. Estaria, J. Faelker, J. Riedinger, A. Robson, B. Taylor *et al.*, "The infrared space observatory (ISO) mission." *Astronomy and Astrophysics*, vol. 315, pp. L27–L31, 1996.

[41] S.-H. Kim, P. Martin, and P. D. Hendry, "The size distribution of interstellar dust particles as determined from extinction," *The Astrophysical Journal*, vol. 422, pp. 164–175, 1994.

[42] K. Takimoto, T. Arai, S. Matsuura, J. J. Bock, A. Cooray, R. M. Feder, P. M. Korngut, Lanz *et al.*, "Polarization spectrum of near-infrared zodiacal light observed with CIBER," *The Astrophysical Journal*, vol. 926, no. 1, p. 6, 2022.

[43] J. Lasue, A. C. Levasseur-Regourd, N. Fray, and H. Cottin, "Inferring the interplanetary dust properties-from remote observations and simulations," *Astronomy and Astrophysics*, vol. 473, no. 2, pp. 641–649, 2007.

[44] A. J. E. Kehoe, "The dynamics of asteroidal dust and structure of the zodiacal cloud," Ph.D. dissertation, University of Florida, 2010.

[45] T. Kelsall, J. Weiland, B. Franz, W. Reach, R. Arendt, E. Dwek, H. Freudenreich, M. Hauser, S. Moseley, N. Odegard *et al.*, "The COBE diffuse infrared background experiment search for the

This work is licensed under a Creative Commons Attribution 4.0 License. For more information, see https://creativecommons.org/licenses/by/4.0/

This article has been accepted for publication in IEEE Transactions on Pattern Analysis and Machine Intelligence. This is the author's version which has not been fully edited and content may change prior to final publication. Citation information: DOI 10.1109/TPAMI.2023.3299526

cosmic infrared background. II. model of the interplanetary dust cloud," *The Astrophysical Journal*, vol. 508, no. 1, p. 44, 1998.
[46] E. Grün, B. A. Gustafson, S. Dermott, and H. Fechtig, *Interplanetary Dust*. Springer, 2012.
[47] L. Smith, F. Roach, and R. Owen, "The absolute photometry of the zodiacal light," *Planetary and Space Science*, vol. 13, no. 3, pp. 207–212, 1965.
[48] Y. Y. Schechner, S. G. Narasimhan, and S. K. Nayar, "Polarization-based vision through haze," *Applied Optics*, vol. 42, no. 3, pp. 511–525, 2003.
[49] S. G. Narasimhan, M. Gupta, C. Donner, R. Ramamoorthi, S. K. Nayar, and H. W. Jensen, "Acquiring scattering properties of participating media by dilution," in *Proc. ACM SIGGRAPH*, 2006, pp. 1003–1012.
[50] M. Tzabari, V. Holodovsky, O. Shubi, E. Eytan, I. Koren, and Y. Y. Schechner, "Settings for spaceborne 3-D scattering tomography of liquid-phase clouds by the CloudCT mission," *IEEE Transactions on Geoscience and Remote Sensing*, vol. 60, pp. 1–16, 2022.
[51] W. A. Shurcliff, *Polarized Light: Production and Use*. Harvard University Press, 1962.
[52] O. Slezák, M. Sawicka-Chyla, M. Divokỳ, J. Pilař, M. Smrž, and T. Mocek, "Thermal-stress-induced birefringence management of complex laser systems by means of polarimetry," *Scientific Reports*, vol. 12, no. 1, p. 18334, 2022.
[53] B. N. Wenny, D. Helder, J. Hong, L. Leigh, K. J. Thome, and D. Reuter, "Pre-and post-launch spatial quality of the Landsat 8 thermal infrared sensor," *Remote Sensing*, vol. 7, no. 2, pp. 1962–1980, 2015.
[54] S. Kabir, L. Leigh, and D. Helder, "Vicarious methodologies to assess and improve the quality of the optical remote sensing images: A critical review," *Remote Sensing*, vol. 12, no. 24, p. 4029, 2020.
[55] J. Hu, A. Razdan, and J. A. Zehnder, "Geometric calibration of digital cameras for 3D cumulus cloud measurements," *Journal of Atmospheric and Oceanic Technology*, vol. 26, no. 2, pp. 200–214, 2009.
[56] V. Jovanovic, M. Smyth, and J. Zong, *Level 1 In-Flight Geometric Calibration Algorithm Theoretical Basis*. JPL Open Repository, 1999.
[57] H. W. Jensen, F. Durand, J. Dorsey, M. M. Stark, P. Shirley, and S. Premože, "A physically-based night sky model," in *Proc. ACM SIGGRAPH*, 2001, pp. 399–408.
[58] M. San, D. Herman, G. Erikstad, M. Galloway, and D. Watts, "COSMOGLOBE: Simulating zodiacal emission with ZodiPy," *arXiv:2205.12962*, 2022.
[59] M. Skrutskie, R. Cutri, R. Stiening, M. Weinberg, S. Schneider, J. Carpenter, C. Beichman, R. Capps, T. Chester, J. Elias *et al.*, "The two micron all sky survey (2MASS)," *The Astronomical Journal*, vol. 131, no. 2, p. 1163, 2006.
[60] A. Ginsburg, B. M. Sipőcz, C. Brasseur, P. S. Cowperthwaite, M. W. Craig, C. Deil, A. M. Groener, J. Guillochon, G. Guzman, S. Liedtke *et al.*, "Astroquery: an astronomical web-querying package in Python," *The Astronomical Journal*, vol. 157, no. 3, p. 98, 2019.
[61] A. M. Price-Whelan, B. Sipőcz, H. Günther, P. Lim, S. Crawford, S. Conseil, D. Shupe, M. Craig, N. Dencheva, A. Ginsburg *et al.*, "The Astropy Project: building an open-science project and status of the v2. 0 core package," *The Astronomical Journal*, vol. 156, no. 3, p. 123, 2018.
[62] M. K. Shepard, *Introduction to Planetary Photometry*. Cambridge University Press, 2017.
[63] M. Versteeg, A. Magalhães, M. Haverkorn, Y. Angarita, C. Rodrigues, R. Santos-Lima, and K. S. Kawabata, "Interstellar polarization survey II: General interstellar medium," *The Astronomical Journal*, vol. 165, p. 87, 2023.
[64] B. Andersson, A. Lazarian, and J. E. Vaillancourt, "Interstellar dust grain alignment," *Annual Review of Astronomy and Astrophysics*, vol. 53, pp. 501–539, 2015.
[65] W. Hiltner, "Polarization of light from distant stars by interstellar medium," *Science*, vol. 109, no. 2825, pp. 165–165, 1949.
[66] C. Leinert, "Zodiacal light—a measure of the interplanetary environment," *Space Science Reviews*, vol. 18, pp. 281–339, 1975.
[67] F. Koreban and Y. Y. Schechner, "Geometry by deflaring," in *Proc. IEEE International Conference on Computational Photography*, 2009, pp. 1–8.
[68] E. Sassoon, Y. Y. Schechner, and T. Treibitz, "Flare in interference-based hyperspectral cameras," in *Proc. IEEE International Conference on Computer Vision*, 2019, pp. 10 174–10 182.
[69] K. Akiyama, A. Alberdi, W. Alef, K. Asada, R. Azulay, A.-K. Baczko, D. Ball, M. Baloković, J. Barrett, D. Bintley *et al.*, "First M87 event horizon telescope results. IV. imaging the central supermassive black hole," *The Astrophysical Journal*, vol. 875, no. 1, p. L4, 2019.

Or Avitan obtained a BSc degree in Electrical Engineering and a BSc degree in Physics from the Technion-Israel Institute of Technology, Israel, in 2014. He is actively engaged in pursuing an MSc degree at the Technion's Viterbi Faculty of Electrical and Computer Engineering. His research interests primarily involve computational photography and machine learning algorithms, with a focus on employing both physics-based and data-driven methodologies.

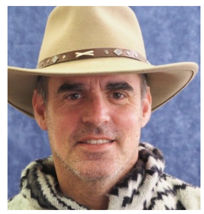

Yoav Y. Schechner is a graduate of the Technion - Israel Institute of Technology: BA (Physics 1990), MSc (Physics 1994), PhD (EE 2000). Afterwards, he was a research scientist at Columbia University (CS). Since 2002, he is a faculty member in the Technion's Viterbi Faculty of Electrical and Computer Engineering. He is the Diane and Mark Seiden Chair in Science. He is a principal investigator and coordinator of the CloudCT project, funded by ERC. In 2010 and 2011 he was a visiting scientist at Caltech and NASA's Jet Propulsion Laboratory (JPL). He won the Best Student Paper Award at CVPR in 2017, the Best Paper Awards at ICCP in 2013 and 2018, and the Distinguished Lecturer Award, Technion 2020. He is the recipient of the Ray and Miriam Klein Research Award, Henry Taub Prize for Academic Excellence, Otto Schwarz Foundation Excellence Award, Norman Seiden Prize for Academic Excellence, Alon and Landau Fellowships. His research interests involve outdoor phenomena and all aspects of imaging.

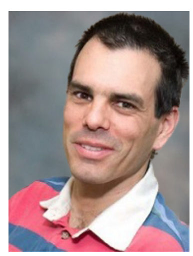

Ehud Behar received all of his degrees from the Hebrew University in Jerusalem, graduating with a PhD in 1999. He was then a post-doctoral scholar at Columbia University in the City of New York. Since 2002, he is a faculty member at the Physics Department of the Technion in Israel, where he was Director of the Asher Space Research Institute (2009-2014), and Dean of the Physics Department (2018-2022). He held Visiting positions at NASA's Goddard Space Flight Center, MD, USA; The University of Maryland College Park, MD, USA; and currently at the MIT Kavli Institute for Astrophysics and Space Research, Cambridge MA, USA. His research interests revolve around experimental high energy astrophysics. He has been closely involved in several space science missions. He is currently a member of the Science Working Group of the Japanese (JAXA) XRISM mission, and on the International Advisory Board of the Italian-European (ASI-ESA) HERMES satellite constellation. He received the Alon fellowship from The Israeli Council of Higher Education, the Krill prize from the Wolf Foundation, a senior NPP fellowship from NASA, and a Madame Curie Global Program Fellowship from the EC.

This work is licensed under a Creative Commons Attribution 4.0 License. For more information, see https://creativecommons.org/licenses/by/4.0/